Stockholm University

Bachelor Thesis

Degree Project in
Geology 15 hp

The occurrence and significance of staurolite in Alpine metapelites: a literature review and thermodynamic modelling

Gonzalo Castaño Jameson

Stockholm 2025

Department of Geological Sciences
Stockholm University
SE-106 91 Stockholm

Abstract

Staurolite is a metamorphic mineral with a complex chemistry, common in Fe-rich and aluminous metapelitic rocks, and regarded as an index mineral of medium-grade metamorphic conditions. In the European Alps, staurolite is widespread. Based on a literature review, I here provide an overview of staurolite and a description of a number of occurrences in the orogen. Complemented with thermodynamic modelling and using data extracted from the literature, I also summarize the effects of the major components on the stabilization of staurolite at depth. The results indicate that staurolite is stable over a metamorphic range of 2.5 to 16 ± 1 kbar and 460 to 666 °C, based on both literature data and thermodynamic modelling. In the Alps, staurolite formed during multiple metamorphic events, including both pre-Alpine (Permian) and Alpine (Eocene) times, having been formed by regional, but also associated with contact metamorphism. Staurolite is present in most paleotectonic domains, which not only reflects the diverse origin of the mineral but also the dynamic nature of the orogen. Additionally, modelling shows the significance of bulk-rock composition in controlling staurolite stability, particularly the effect of Fe and Al in expanding the pressure-temperature (*P–T)* stability field. This reinforces the importance of protolith composition in interpreting metamorphic grade based in staurolite stability.
Finally, staurolite can host appreciable amounts of lithium (up to ~0.3 wt%). In this context, the thesis also aims to investigate the occurrence and behaviour of staurolite in order to add to the broader understanding of the large-scale lithium cycle—an increasingly important metal.

Table of Contents

Introduction 5

Methods 6

- Literature review 6
- Petrography 6
- Bulk rock composition 7
- AFM ternary plot (projection) 7
- Mineral chemistry 7
- Thermodynamic modelling 8

Results 9

- Staurolite in the field 9
- Staurolite under the microscope: optical properties and textural characteristics 9
- Growth and breakdown reactions of staurolite in metapelites 11
- Bulk-rock composition 15
- Staurolite composition 15
- Occurrence and stability (P-T conditions) of staurolite in metapelites: a survey in the Alpine realm 15
  - *Eastern Alps: Wölz and Rappold Complexes* 15
  - *Campolungo metapelites of the Simano nappe, Lepontine Alps* 18
  - *Monte Rosa Nappe, central Alps* 19
  - *Contact aureole of the Vedrette di Ries pluton* 20

Discussion 21

- Relative influence of Al, Fe, and Mg on staurolite stability 22
- 24
- Petrographical evidence in staurolite-Al_2SiO_5 relations for polymetamorphism and tectonic evolution 24
- Lithium 26

Conclusions 26

Acknowledgements 27

Bibliography 28

Supplementary Material 30

List of Figures

Figure 1. Staurolite and its crystal structure 6
Figure 2. Schematic tectonic map of the Alps showing the location of studied staurolite-bearing metapelites.....9
Figure 3. Prismatic staurolite porphyblasts in a mica schist. 10
Figure 4. Staurolite in thin section. 11
Figure 5. Simplified petrogenetic grid showing curves and reactions involving staurolite. 14
Figure 6. AKFM (Al_2O_3-K_2O-FeO-MgO) chemographic ternary diagrams showing the changes in topology resulting from the numbered reactions in Figure 4. 15
Figure 7. Diagrams showing the modal abundances of staurolite. 19

Figure 8. Metapelites from the Monte Rosa nappe, SEM image, and phase diagram. ..20
Figure 9. Thin section of metapelite from contact aureole of the Vedrette di Ries pluton and phase diagram. 21
Figure 10. Pseudosection calculated for sample MF161 from Janots et al. (2008) in the system MnNCKFMASHTO. 22
Figure 11. Pseudosection calculated for sample MF307 from Janots et al. (2008) in the system MnNCKFMASHTO. 23
Figure 12. Pseudosection for sample MF315 in the system MnNCKFMASHTO from Janots et al. (2008). 24
Figure 13. Staurolite stability fields superimposed in P-T space. 25
Figure 14. A(K)FM ternary projection showing the variability in metapelite compositions. 26

List of Tables

Table 1. Compilation of major oxide compositions (wt%) of metapelite samples from the Central and Eastern Alps. 17
Table 2. Compiled (EPMA) data of average staurolite compositions and cation proportions from Alpine metapelites. 18
Table 3. Ratios of the AFM components. Calculated from values in Table S1 in supplementary material. 26

Introduction

Staurolite is a medium-temperature, medium-pressure metamorphic mineral, commonly found in metapelitic (metamorphosed fine-grained sediments) rocks worldwide. It typically appears as a dark reddish-brown, twinned, often prismatic, hard mineral (Figure 1), frequently associated with other metamorphic minerals such as biotite, garnet, kyanite and muscovite. Staurolite is favored in highly aluminous and Fe-rich rocks, commonly in metamorphosed mudstones and shales, and more rarely in metabasalts and even metamorphosed ultrabasic rocks of appropriate composition (Borisova et al., 2022; Ibarguchi et al., 1991).

Staurolite is a mineral with complex chemistry and structure. However, it can be broadly described as a monoclinic, aluminous nesosilicate with limited solid solution between Fe and Mg, with the simplified, ideal chemical formula $(Fe, Mg)_2Al_9Si_4O_{22}(OH)_2$ (Blatt et al., 2006). Compositionally, staurolite sits close to the Fe end of the Fe-Mg range, although Mg-rich varieties exist, associated with high pressure metabasalts (Borisova et al., 2022; Janák et al., 2015). Additionally, Zn-rich (6.0 – 7.5 wt %), Cr-rich (>6 wt%), and Co-bearing occurrences have been documented (Miyake, 1985; Ibarguchi et al., 1991; Bringhurst and Griffen, 1986). Staurolite is also noted for containing significant amounts of lithium (0.048 wt%, as reported by Gieré et al., (2011)), being an important Li host in metapelites.

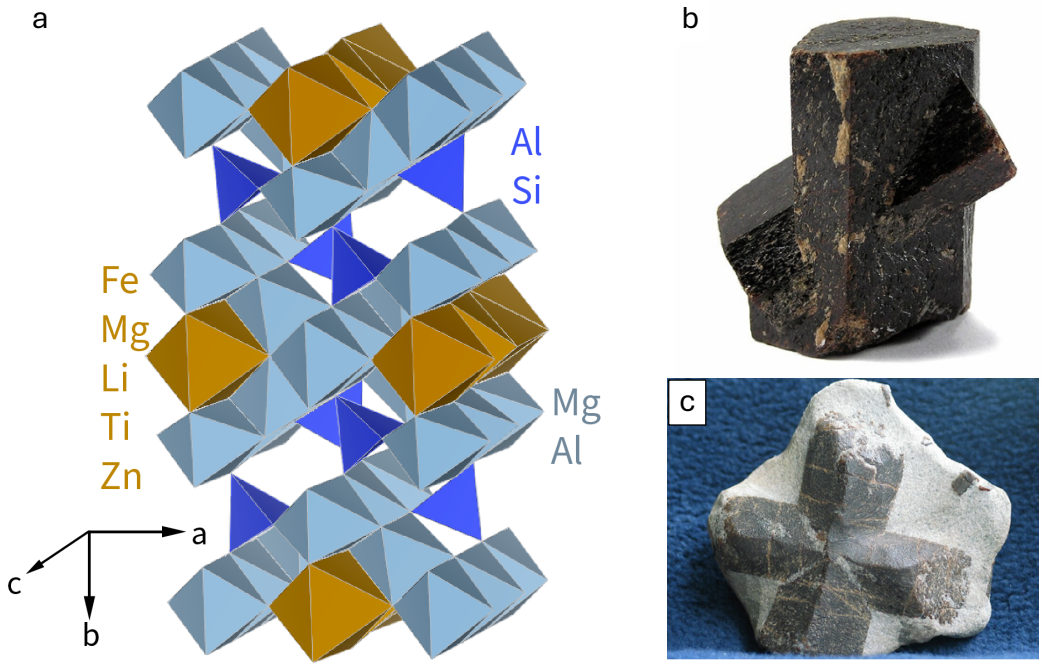

Figure 1. a) Crystal structure of staurolite showing isolated SiO_4^{-4} tetrahedra (dark blue), characteristic of nesosilicates. Si^{+4} cations are partially replaced by Al^{+3}. Octahedral structures accommodating other cations present in staurolite are also shown. AMC file based on Hawthorne et al. (1993), visualized in VESTA; available at RRUFF database. b) A well-formed dark, prismatic crystal with a characteristic cross-twin at 60°. (Lavinsky, available at www.mindat.org). c) Cross-twinned staurolite crystal at 90°. Both twinning orientations are common. (Darski, from commons.wikimedia.org).

In metapelites with typical compositions, some estimates place staurolite within temperatures of ~530–680 ºC and pressures ranging from ~2.0 to 14 kbar (Spear and Cheney, 1989; Winter, 2014a), broadly corresponding to the amphibolite facies. Rocks subjected to regional, medium-pressure metamorphism are likely to enter this temperature range, making staurolite-bearing mineral assemblages common in regionally metamorphosed terranes.

Due to its relatively narrow stability range, staurolite is classified as an index mineral, serving as an indicator of metamorphic grade in Barrovian-type metamorphism (Blatt et al., 2006). In this context, the progression of minerals—chlorite, biotite, garnet, staurolite, kyanite, and sillimanite—develops with increasing grade, each phase marking a metamorphic zone associated with a stable mineral assemblage. Less frequently, staurolite also forms in high-Al, Fe-rich metapelites during low-pressure contact metamorphism, often in association with chlorite, chloritoid, biotite or andalusite.

The aim of this thesis is 1) to describe staurolite and its occurrence within the Alpine context, based on a comprehensive literature review, and 2) to evaluate the role of major chemical components in stabilizing staurolite at depth using thermodynamic modelling based on data extracted from the literature. Given the prevalence of staurolite in metapelites, understanding its behavior during metamorphic processes and its relationship to specific rocks and mineral assemblages in Alpine geology can greatly aid in constraining the metamorphic history of many localities through extrapolation. Furthermore, due to its potential to accommodate lithium (Li), studying staurolite stability can provide insights into the fate of this important metal after its release during mineral breakdown, as well as the role of staurolite as a potential source at depth of near-surface Li enrichment.

Methods

Literature review

The aim of the literature review was to compile sufficient data to summarise the occurrence of staurolite in the European Alps and attempt to build a general overview on this mineral. What are the main (optical and chemical) features of staurolite in metapelites? What are the main factors (e.g., chemical and bulk rock composition, pressure, temperature) controlling the stability of this mineral in Alpine metapelites? My thesis aims to answer to these questions. Therefore, I extensively focused my literature review on published studies on the Alps that described staurolite. In addition, I have incorporated relevant data on this mineral from petrology textbooks. Finally, I have also conducted research on the Alpine geology. This is a key point in order to fully understand the occurrence of staurolite in these rocks.

Petrography

The description of staurolite under the microscope was based on the most common properties used to identify minerals in thin section: shape, habit, relief, cleavage,

absorption colours, birefringence. This information was extracted from well-known publications, such as the atlases by W.S. MacKenzie and co-authors, and online materials. Both plane- and cross-polarized images were used from these sources, citing the used relevant works in the captions and/or in the text. Images of staurolite were selected on the basis of their quality and with the aim to illustrate the mentioned properties.

Bulk rock composition

A table (Table 1) reporting the bulk rock compositions of samples containing staurolite was compiled. Samples have been collected in several localities in the Alps (Figure 2) and studied by Gaidies et al. (2006), Janots et al. (2008), Gieré et al. (2011), and Vaughan-Hammon et al. (2021). The bulk compositions were obtained by conducting X-ray fluorescence analysis (XRF) on powdered rock samples. The sample amounts varied by study, with a total range of 10 g to ~1300 g. A complete description of the methods is provided in the respective papers and their appendices.

AFM ternary plot (projection)

A ternary diagram (Figure 14) was constructed using the molecular proportions of Fe, Mg, and Al oxides, selected for their significant influence on mineral stabilization in metapelites. Since the diagram assumes that all K_2O partitions into muscovite, 3 moles of Al_2O_3 per 1 mole of K_2O are subtracted from the total Al_2O_3, following muscovite's stoichiometric formulation. The AFM plane is thus projected from muscovite, as well as from quartz and water. The data, derived from the weight percent compositions in Table 1, were recalculated to molecular proportions (see Table S4 and S5, and Figure S1 in the supplementary materials). The plotting template was downloaded from https://serc.carleton.edu/details/files/19001.html.

Mineral chemistry

A table (Table 2) of chemical compositions (expressed as oxides) of staurolite was also similarly compiled, extracting data from Gieré et al. (2011) and Vaughan-Hammon et al. (2021) (Figure 2). Gieré et al. determined mineral compositions by electron probe micro-analysis (EPMA), with an acceleration potential of 15 kV and beam current of 20-100 nA. In this study, the chemical compositions of staurolite are reported as averages of a random selection of crystals: 14 crystals from one rock sample and 69 crystals from another one. Laser ablation inductively coupled plasma mass spectrometry (LA-ICP-MS) was additionally used for analysing the composition of trace elements, such as Li_2O. This element is reported in the compiled table. Vaughan-Hammon et al. (2021) also obtained mineral compositions by EPMA at 15 kV and 15-20 nA on 12 crystals of staurolite. Further details on the methods followed for mineral chemistry are available in the respective papers and their appendices.

Thermodynamic modelling

Pseudosections in the system MnNCKFMASHTO (representing element oxides) were constructed using the software Theriak-Domino (De Capitani and Petrakakis, 2010), which depict stable mineral assemblages for a specific bulk rock composition as a function of temperature and pressure. The bulk rock compositions used for these calculations are those of samples MF161 and MF307 from Janots et al. (2008) (see Table 1). Fe^{3+} concentration was chosen as 5% of FeO* based on the approach of Nosenzo et al. (2011) and Manzotti et al. (2018) for metapelites. The data set used is the thermocalc dataset 55 modified by Pavel Pitra (tcds55_pp05), originally developed by Holland and Powell (1998) and converted to Theriak-Domino format by D.K. Tinkham, 2012. The activity-X models used in this dataset are listed in Appendix S1 in the Supplementary materials section.

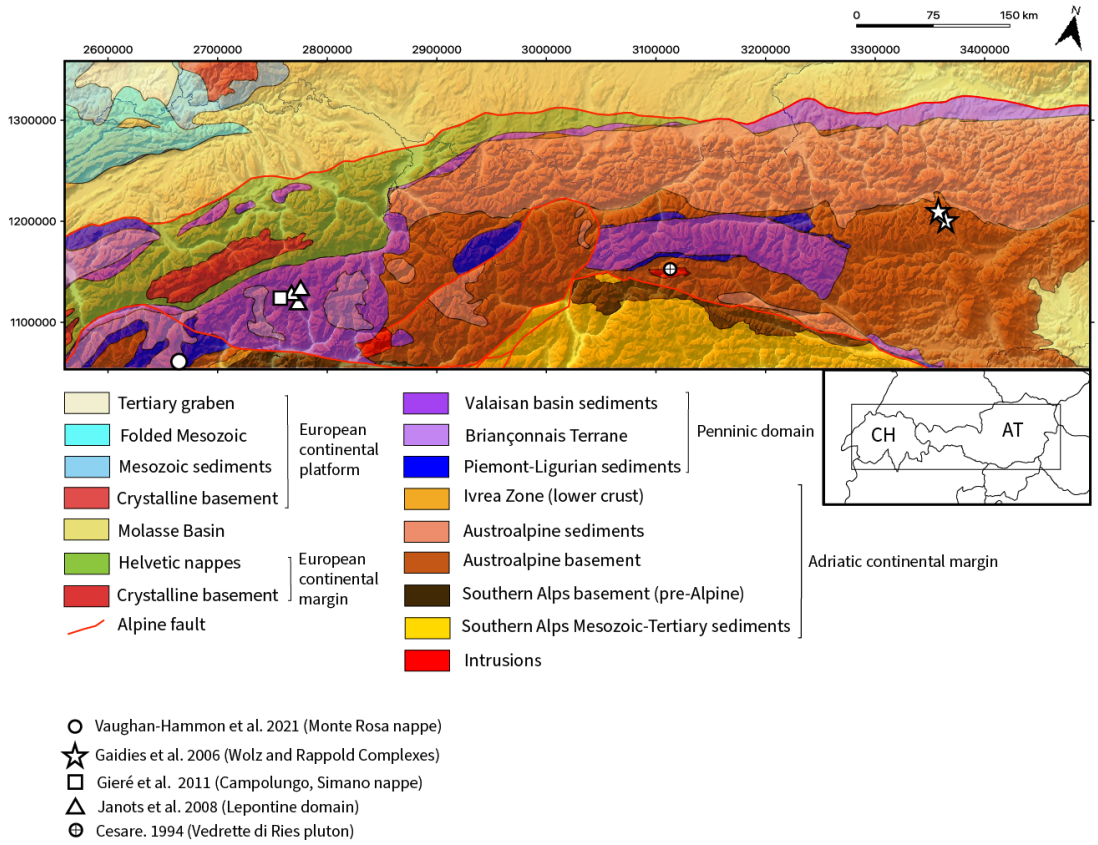

Figure 2. Schematic tectonic map of the Alps showing the location of studied staurolite-bearing metapelites. Modified from Handy et al. (2010) and the *Tectonic Map of Switzerland*, 1:500,000 (University of Bern; published by the *Office federal des eaux et de la géologie)*.

Results

Staurolite in the field

In the field, staurolite occurs primarily in regionally metamorphosed terranes, typically found in medium grade metapelitic rocks, commonly schists and gneisses, associated with other silicates such as garnet, kyanite or sillimanite, biotite, muscovite and quartz. It often occurs as prismatic, porphyroblastic crystals, being readily identifiable from the surrounding matrix due to its relatively large size; and it can exhibit an elongated habit, as well as romb- or lozenge-shaped crystals when properly oriented. Cross twinning is arguably the most distinctive marker for its identification (Figure 3). Its colour is typically dark to reddish brown, but it can also be yellowish brown. The mineral's hardness, between 7 and 7.5 in Mohs scale, and vitreous luster, can also serve as useful diagnostic properties.

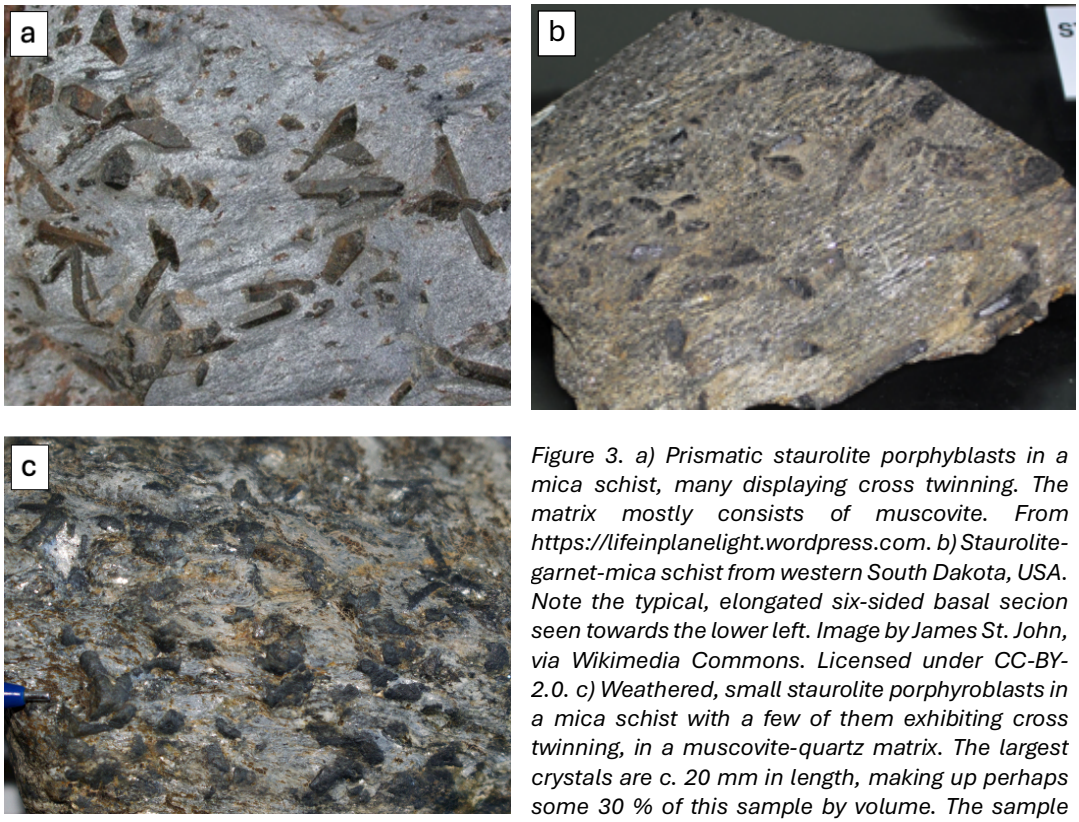

Figure 3. a) Prismatic staurolite porphyblasts in a mica schist, many displaying cross twinning. The matrix mostly consists of muscovite. From https://lifeinplanelight.wordpress.com. b) Staurolite-garnet-mica schist from western South Dakota, USA. Note the typical, elongated six-sided basal secion seen towards the lower left. Image by James St. John, via Wikimedia Commons. Licensed under CC-BY-2.0. c) Weathered, small staurolite porphyroblasts in a mica schist with a few of them exhibiting cross twinning, in a muscovite-quartz matrix. The largest crystals are c. 20 mm in length, making up perhaps some 30 % of this sample by volume. The sample likely belongs to Pontis Nappe, within the Briançonnais tectonic unit and it was collected from Col du Grand-Saint-Bernard in the Swiss Alps, Swiss Coordinates (LV95): 2'580'397, 1'079'918.

Staurolite under the microscope: optical properties and textural characteristics

Staurolite is a high, positive relief mineral, with an intermediate refractive index (β) of 1.75 - 1.753, and a birefringence range of 0.012 - 0.014, as reported by Yardley et al. (1990) and 0.009 - 0.015 by mindat.org. It is biaxial positive, shows parallel extinction and a weak cleavage. Lozenge or diamond, six-sided shapes are typical of basal sections, while an elongated habit is common when observed perpendicular to the c-axis. It is also known for its yellow absorption colours in plane polarised light, but importantly, by its pleochroism, ranging from colourless to yellow to pale yellow, often used as a diagnostic

property of this mineral. A large number of small inclusions, commonly of quartz, are often seen in staurolite, giving it a patchy or mottled texture towards the interior of the

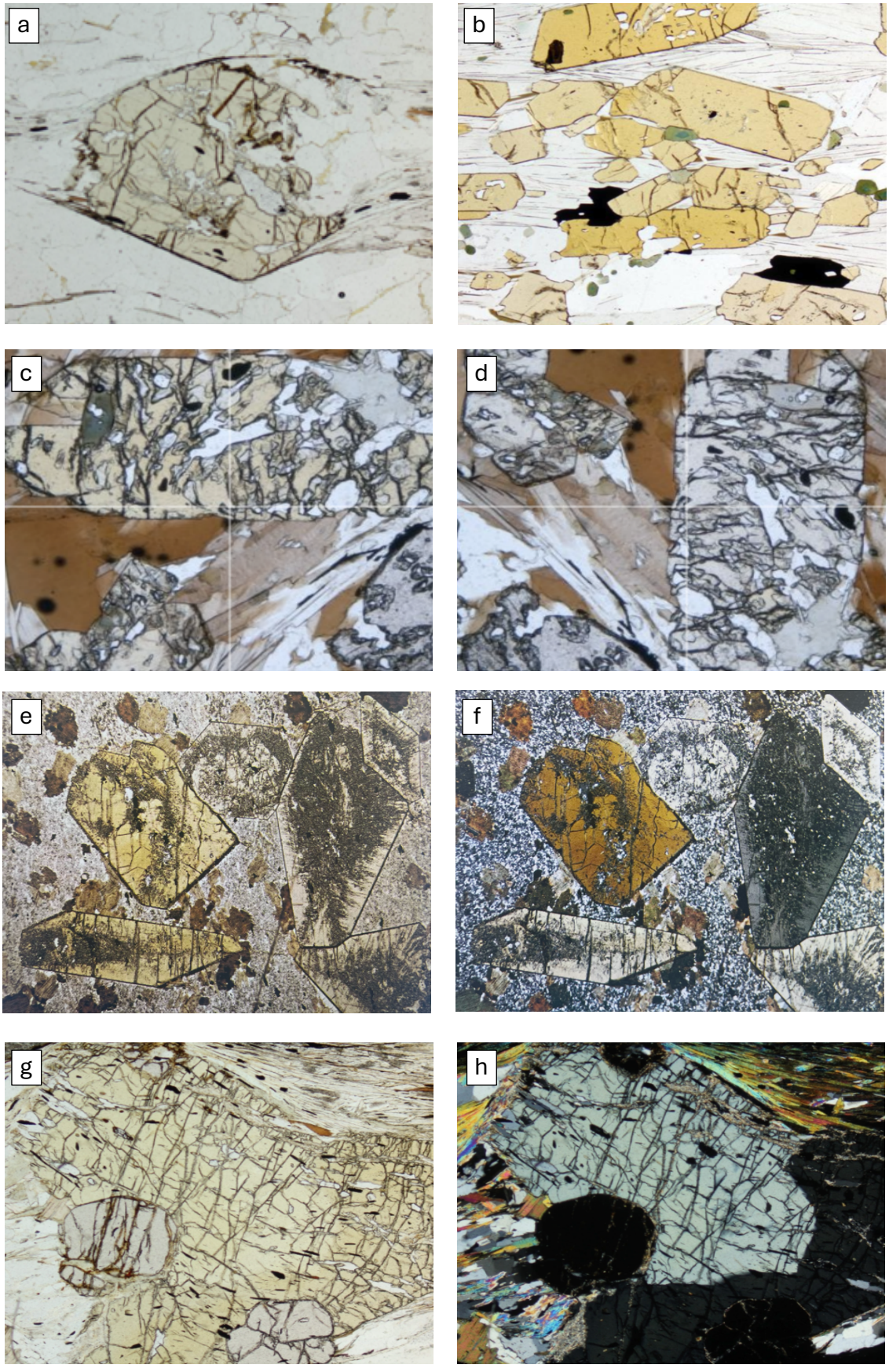

Figure 4. a) Subhedral basal section of a pale yellow staurolite porphyroblast. Despite the replacement and deformation, the diamond shape of the crystal is still clearly visible. The other minerals are quartz and muscovite. Posada Valley, Sardinia, Italy; 5 mm field of view, PPL. Image from www.geologyistheway.com. b) Sheared and broken yellow staurolite crystals displaying a typical elongated habit. Matrix of muscovite and quartz. Posada Asinara, Sardinia, Italy; 5 mm field of view, PPL. From www.alexstrekeisen.it. c) Pale yellow staurolite crystal (upper half) exhibiting pleochroism when rotated 90 ° clockwise to produce a pale, greyish grain in (d). Other minerals in the section are garnet, muscovite, biotite, feldspar and quartz. Elf Hillock, Glen Clova, Scotland; 2 mm field of view, PPL. Images from www.virtualmicroscope.org. e) PPL section showing several large porphyroblasts of staurolite and smaller biotite. A dense concentration of inclusions, combined with the high relief of staurolite results in the patchy texture seen in the interior of the crystals. The high relief is also evident in the thick edges of some of the crystals. f) Same section in cross polarized light (XPL) showing the low interference colours of staurolite. Waddy Lake, Saskatchewan, Canada; magnification x 20. From Yardley et al. (1990). g) Pale yellow staurolite porphyroblast with small inclusions of quartz and an opaque mineral and larger garnet inclusions. The irregular shape of this crystal is caused by cross twinning. 5 mm field of view. PPL. From www.alexstrekeisen.it. h) Same as (g) but in XPL. The twinning is evident here with one twin almost at extinction towards the lower right of the field of view and the other showing low interference colours.

crystals (Figure 4e, f). In cross polarisation, it shows low order interference colours (Figure 4f, h), from white to grey, to first order yellow. However, first-order red may also appear due to the influence of the mineral's pleochroism (Yardley et al., 1990).

Growth and breakdown reactions of staurolite in metapelites

Several reactions for the formation and breakdown of staurolite in metapelites have been proposed in the literature, each showing varying degrees of consistency between thermodynamic equilibrium models and natural observations (see Pattison and Spear, 2018). Additionally, since the occurrence of specific reactions depends on metamorphic grade and bulk rock composition, they may vary significantly between (or even within) metamorphic sequences. This section is a summary outlining the reactions involving the formation and breakdown of staurolite as described in Winter (2014). The reactions pertain to rocks within the typical range of pelite compositions, based on the table of *Chemical Compositions of Shales and Metapelites* (with references therein) presented in the same text, and conform to the medium metamorphic field gradient described by Winter (2014) and illustrated in the petrogenetic grid in Figure 5. Because petrogenetic grids typically display only discontinuous reactions—those occurring at a specific metamorphic grade—only this type of reaction is listed below. However, it should be emphasized that phases can also form and break down through continuous reactions, occurring over a range of metamorphic conditions.

Following the medium metamorphic field gradient in Figure 5 (red arrow), the first staurolite-forming reaction encountered is the univariant curve (dashed) producing Fe-staurolite from Fe-chloritoid reacting with kyanite. This reaction is not numbered in Figure 5 because it will only be manifested in unusually Fe-rich rocks, and thus outside the range of average pelite compositions (Figure 6, shaded fields). In the chemographic ternary diagrams, this reaction would result in the appearance of Fe-rich staurolite between Fe-rich chloritoid and kyanite along the A-M edge. A similar situation occurs at higher temperature, at the next dashed univariant reaction curve in Figure 5 (also not numbered), which marks the disappearance of Fe-rich chloritoid as it is consumed to produce Fe-rich staurolite and Fe-rich biotite (annite). However, a more plausible reaction to occur in rocks of a more common composition (i.e., those with an added Mg component) is:

$$Cld + Ky = St + Chl (+ Qtz + H_2O) \quad (1)$$

This reaction is labelled as number 1 in and marks the *true* introduction of staurolite, or the staurolite-in isograd, in these rocks. In the chemographic triangular diagram labelled as B in Figure 6, reaction (1) is represented by a tie-line flip from Cld-Ky (dashed line) to St-Chl, placing these rocks in the *lower* staurolite zone of the amphibolite facies (Winter, 2014b). Chemographic diagram B illustrates how mineral assemblages in staurolite-bearing rocks within this composition (shaded region) could develop either Cld-St-Chl or St-Ky-Chl (both assemblages containing H_2O, quartz, and muscovite), depending on bulk rock composition, as the shaded region spans both subtriangles containing staurolite.

With increasing grade, the next encountered reaction at point 2 in Figure 5 is:

$$Cld (+ Qtz) = Grt + Chl + St + H_2O \quad (2)$$

This reaction marks the disappearance of the most Mg-rich chloritoid (now represented by a single point in Figure 6, diagram C, where the Mg concentration has increased due to reactions producing garnet and staurolite, both with higher Fe content) from the average metapelite and introduces garnet. However, in common metapelites richer in Fe and with medium Al content (plotting near the chlorite Fe endmember in diagram C), in which garnet became stable at an earlier stage, this reaction marks the first appearance of staurolite. Because chloritoid not only disappears from the rocks in question but also from the chemographic diagram, this represents a terminal reaction. This is shown as the disappearance of the three dashed tie-lines (Figure 6, diagram C) connecting the now single-point Cld to St, Grt and Chl, resolving into a larger subtriangle with the three latter phases at its vertices.

Based on the limits of the shaded region in diagram C, this reaction will only be manifested in rocks with the most Fe-rich bulk rock compositions within the average metapelite, and thus only these compositions will have coexisting garnet and staurolite at this grade.

At ~590 °C, reaction (3) is encountered at point 3 in Figure 5:

$$Grt + Chl (+ Ms) = St + Bt (+ Qtz + H_2O) \quad (3)$$

In Figure 6, diagram D, the reaction is represented by a tie-line flip between Grt-Chl (dashed) and St-Bt, and marks the transition to the staurolite zone of the amphibolite facies (Winter, 2014b) —no longer the *lower* staurolite zone. This reaction introduces staurolite to low-Al, common metapelites, and indeed, to most metapelites with average composition, or within the shaded field in diagram D. Similarly, it introduces biotite to high-Al, common metapelites, enabling the coexistence of staurolite and biotite above this grade, as a result of the breaking of the Grt-Chl "join" (see Albee, 1972). Reaction (3) is also significant due to the large portion of the diagram it affects; it occurs across a broader range of bulk rock compositions and is therefore more likely to be observed in the field (Albee, 1972).

Following the medium metamorphic field gradient, at ~630 °C, point 4 in Figure 5, the reaction:

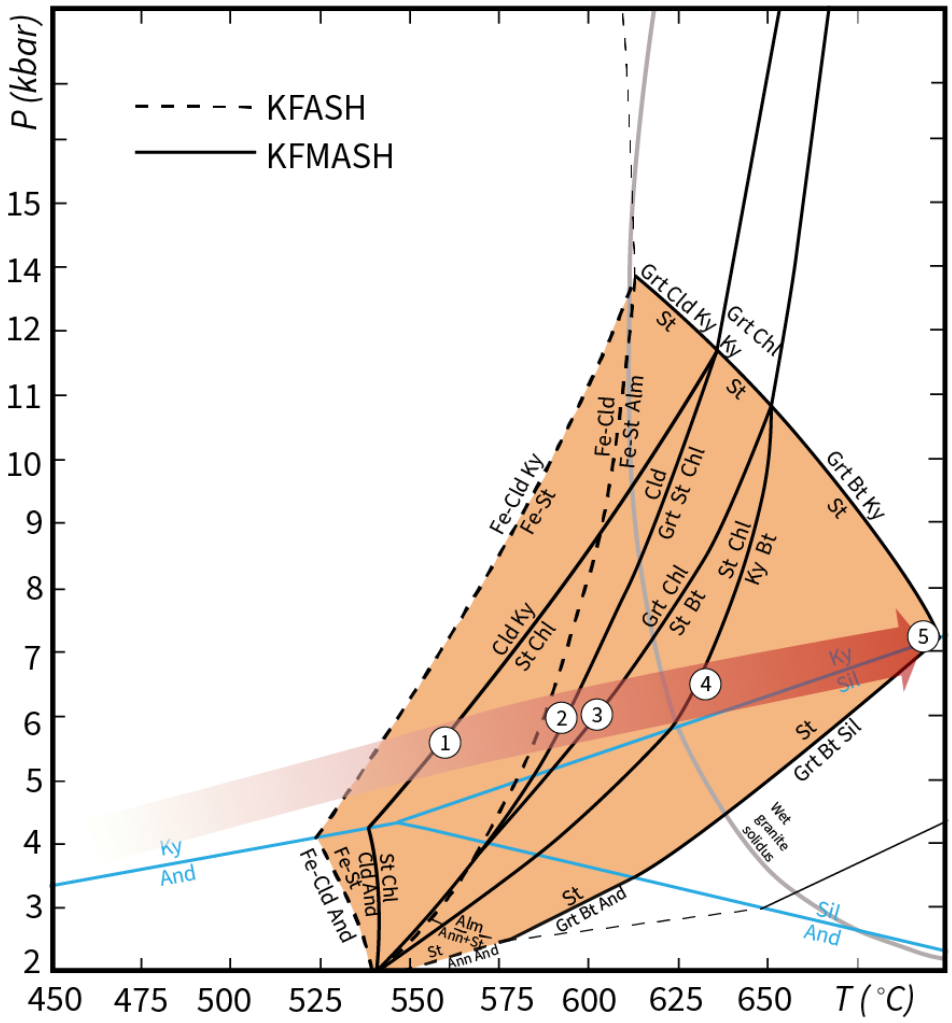

Figure 5. Simplified petrogenetic grid showing curves and reactions involving staurolite, the stability fields of the three aluminosilicates—kyanite, andalusite, and sillimanite—and the wet granite solidus (grey solid curve). The orange-coloured area represents the staurolite stability field, and the red arrow indicates a medium metamorphic field gradient. Numbers correspond to reactions described in the text. All other reaction curves have been omitted for simplicity. The grid corresponds the systems KFASH (K_2O-FeO-Al_2O_3-SiO_2-H_2O, dashed curves) and KFMASH (with the added MgO component, solid black curves). Only discontinuous reactions are shown in this grid, and therefore a limited number of reactions for the formation and breakdown of staurolite are represented. Ann = Fe-biotite, Alm = Fe-garnet. Modified from Winter (2014).

$$St + Chl\ (+ Ms + Qtz) = Ky + Bt\ (+ H_2O) \qquad (4)$$

stabilizes kyanite in common pelites and consumes staurolite in the most Mg-rich, lowest-Al rocks within the shaded field, represented by a tie-line flip between the St-Chl (dashed) to Ky-Bt (Figure 6, diagram E). In these rocks, therefore, staurolite is first broken down at this grade.

The ultimate stability limit for staurolite, according to the petrogenetic grid of and following the specified metamorphic *P-T* path, occurs at point 5, and is represented by the reaction:

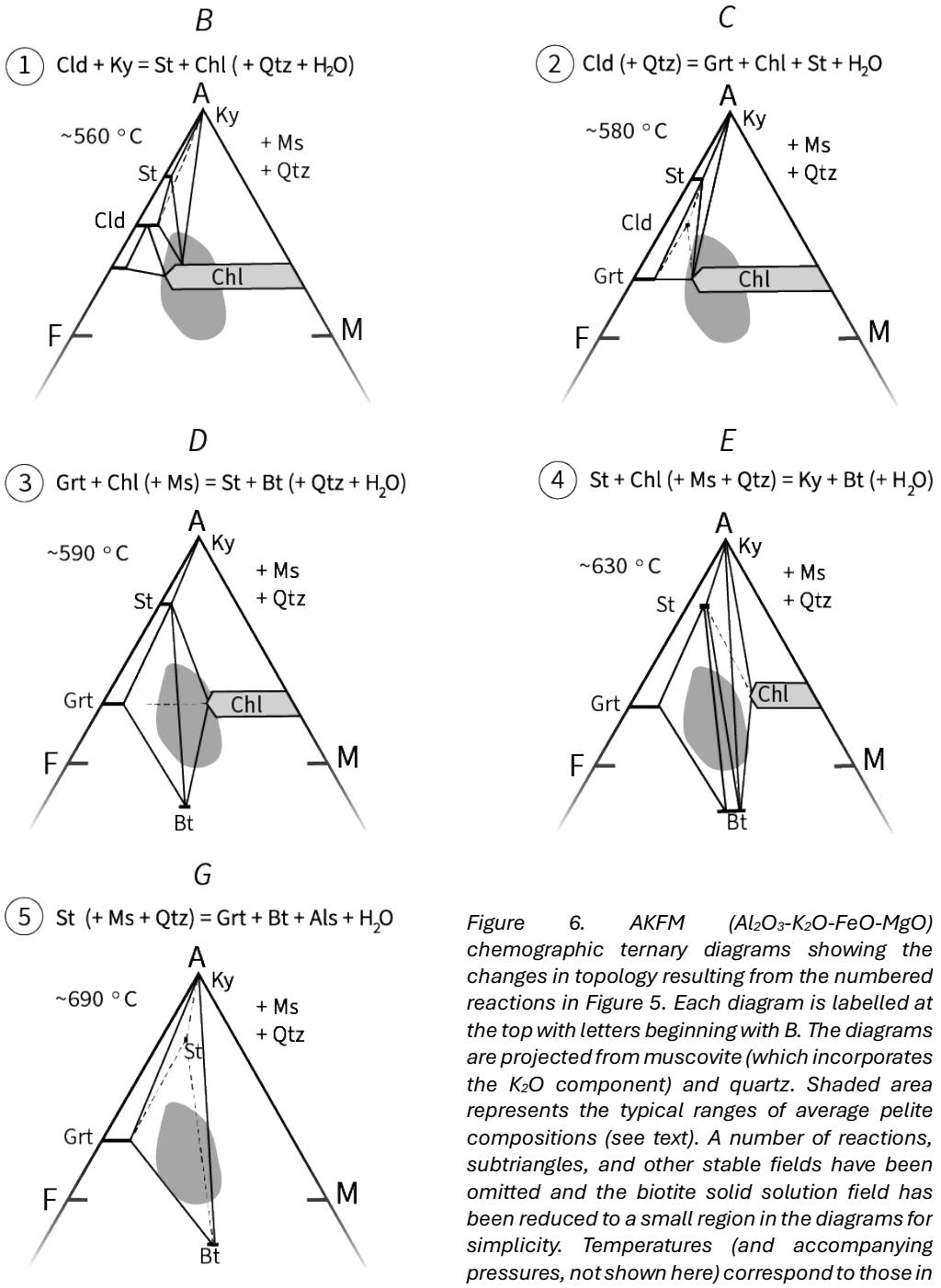

Figure 6. AKFM (Al_2O_3-K_2O-FeO-MgO) chemographic ternary diagrams showing the changes in topology resulting from the numbered reactions in Figure 5. Each diagram is labelled at the top with letters beginning with B. The diagrams are projected from muscovite (which incorporates the K_2O component) and quartz. Shaded area represents the typical ranges of average pelite compositions (see text). A number of reactions, subtriangles, and other stable fields have been omitted and the biotite solid solution field has been reduced to a small region in the diagrams for simplicity. Temperatures (and accompanying pressures, not shown here) correspond to those in Figure 5. Modified from Winter (2014).

$$\text{St (+ Ms + Qtz)} = \text{Grt + Bt + Als + } H_2O \qquad (5)$$

marking the disappearance of staurolite in common pelites and also from the chemographic ternary diagram (Figure 6, diagram G). This is thus a terminal reaction representing the staurolite-out isograd and is shown in diagram G as the disappearance of the most Mg-rich staurolite—now reduced to a point—along with the dashed tie-lines emanating from it, resolving into the Grt-Ky-Bt subtriangle. Based on the ternary diagram,

common metapelites above this isograd are therefore expected to consist of a stable assemblage of mainly garnet, kyanite, and biotite (plus quartz and muscovite).

Bulk-rock composition

Bulk-rock compositions of Alpine staurolite-bearing metapelites, based on those reported by Gaidies et al. (2006), Janots et al. (2008) and Gieré et al. (2011) are presented in Table 1. In both Gaidies et al. (2006) and Gieré et al. (2011), the reported analyses show minimal variation compared to common pelitic compositions [e.g. North American Shale Composite (NASC) (Condie, 1993; Gromet et al., 1984), the average pelite of Symmes and Ferry, 1991)]. The metapelites studied by Gaidies et al. (2006) show slight enrichments in Fe relative to Mg and Al relative to Ca. In contrast, those analyzed by Gieré et al. (2011) display only a notably low Ca content compared to NASC.

Staurolite composition

Similarly, staurolite compositions from the Alps were compiled from Gieré et al. (2011) and Vaughan-Hammon et al. (2021), and are presented in Table 2. In both studies, staurolite is enriched in Fe, with Fe/(Mg+Fe) values of 0.8 and 0.68-0.74, respectively, as well as in Zn, particularly in the staurolites analyzed by Vaughan-Hammon et al. (2021) (~1.0 Zn a.p.f.u.). Gieré et al. (2011) also reports that staurolite contains the highest Li concentrations among the studied minerals, exceeding 200 ppm.

Occurrence and stability (P-T conditions) of staurolite in metapelites: a survey in the Alpine realm

This section provides an overview of several, but by no means all, staurolite occurrences in the European Alps, including a short account of the geological context and history of some of the host rocks. It also includes a number of *P-T* estimates, as reported in the respective source papers, along with some simplified thermodynamic models presented in those studies.

Eastern Alps: Wölz and Rappold Complexes

The Wölz and Rappold Complexes are part of the Austroalpine basement in the Eastern Alps, representing the upper plate under which the former European margin and Penninic Oceans were subducted during the Cretaceous and Tertiary periods. These complexes have experienced multiple metamorphic events, including pre-Alpine metamorphism (Gaidies et al., 2006) (Figure 2). In metapelites from the Wölz Complex, staurolite often occurs intergrown with 8 mm-long kyanite porphyroblasts in a matrix of muscovite, quartz, rutile, biotite and plagioclase. Staurolite in these rocks is believed to have formed as part of a Permian mineral assemblage (Gaidies et al., 2006; Prenzel and Abart, 2009). In the Rappold Complex metapelites, staurolite occurs as small, 1 mm-sized crystals in a matrix of muscovite, biotite, plagioclase, quartz, ilmenite and tourmaline as the major phases and shows abundant inclusions of graphite. Garnet isopleth thermobarometry by

Gaidies et al (2006) on incipient first-generation garnets in equilibrium with staurolite of the Rappold Complex yielded *P-T* estimates of ~5.3 ± 0.3 kbar and 525 ± 15 °C.

Table 1. Compilation of major oxide compositions (wt.%) of metapelite samples from the Central and Eastern Alps.

Study	Gaidies et al. (2006)			Janots et al. (2008)							Gieré et al. (2011)								
Domain	Eastern Alps			Central Alps							Central Alps								
				Quartenschhiefer and Bünderschiefer															
Unit	Wölz Complex		Rappold Complex	Lucomagno				Piora	Molare		Campolungo								
Sample	12F03	29F03B	35F03	MF161	MF307	MF315	APi0413	SPi0306	SMo0407	AMo0410	Leit 3	Leit 8	Leit 10	Leit 300	Leit 300a	Leit 400	Leit 400a	Leit 400b	Leit 900
Wt% oxides																			
SiO_2	57.51	64.04	48.02	52.90	59.00	54.60	47.75	53.28	49.84	59.29	53.90	53.20	61.00	55.60	56.10	61.80	50.40	50.50	60.50
TiO_2	1.19	0.83	0.97	1.30	0.80	1.50	1.06	1.56	1.05	0.92	1.13	1.10	0.93	1.06	1.07	0.83	1.16	1.17	0.89
Al_2O_3	20.98	18.02	26.21	29.70	20.30	27.90	25.22	26.35	25.41	21.92	24.60	24.10	20.60	23.80	23.60	20.00	26.10	25.60	20.50
FeO*	8.53	6.93	9.47	4.70	6.80	10.30	8.87	8.32	10.32	7.38	7.54	8.86	6.74	7.53	7.34	5.99	8.19	8.30	6.85
MnO	0.11	0.10	0.06	0.05	0.02	0.05	0.02	0.04	0.79	0.34	0.10	0.11	0.09	0.12	0.12	0.06	0.12	0.12	0.11
MgO	2.28	2.10	2.61	3.90	5.90	1.40	6.72	1.59	2.40	1.93	2.00	2.28	1.78	1.82	1.98	1.96	2.16	2.64	2.00
CaO	0.46	0.52	0.36	0.35	1.80	0.31	1.38	1.32	1.65	1.05	0.27	0.20	0.28	0.30	0.29	0.28	0.35	0.54	0.28
Na_2O	1.23	1.06	0.64	2.20	1.60	1.80	4.30	3.11	3.05	2.26	1.22	1.08	1.03	1.19	1.26	1.31	1.90	1.98	0.98
K_2O	3.73	3.43	5.84	3.10	3.51	1.65	4.70	3.64	1.84	3.10	4.82	4.61	3.96	4.53	4.69	4.05	4.78	4.38	4.30
P_2O_5				0.09	0.16	0.11	0.34	0.02	0.04	<0.01	0.10	0.07	0.10	0.10	0.09	0.14	0.11	0.10	0.11
LOI				3.90	1.90	1.90	3.44	3.02	1.61	1.83	2.65	2.20	1.90	2.55	2.35	2.60	2.85	2.55	2.40
Total	100.16	100.82	99.04	99.76	100.08	100.17	101.70	100.26	99.14	100.03	99.20	98.90	99.20	99.40	99.70	99.70	99.00	98.50	99.70

LOI: Loss on ignition

All Fe recalculated as $FeO^* = FeO + 0.8998 \cdot Fe_2O_3$

Table 2. Compiled (EPMA) data of average staurolite compositions and cation proportions from Alpine metapelites.

Study	Gieré et al. (2011)	Gieré et al. (2011)	Vaughan-Hammon et al. (2021)
Peak P-T conditions	8.5 kbar 667 °C	4.6 kbar 550 °C	16 ± 2 kbar 585 ± 20 °C
Domain	Central Alps	Central Alps	Central Alps
Unit	Campolungo	Campolungo	Monte Rosa
Rock Type	Metapelite	Metapelite	Metapelite
Sample	Leit 8c	Leit 8g	19MR-33
SiO_2	28.60	28.00	28.19
Al_2O_3	53.60	53.50	52.91
Cr_2O_3	n.a.	0.04	
TiO_2	0.61	0.63	0.33
FeO_{tot}	13.40	13.90	9.59
MnO	0.03	0.04	0.03
NiO	n.a.	0.02	
ZnO	0.36	0.35	4.74
MgO	1.89	1.90	1.81
CaO	n.a.	<0.01	0.01
Na_2O	n.a.	0.01	0.09
K_2O	n.a.	<0.02	0.01
H_2O	1.83	1.72	
Total	100.29	100.11	97.71
Oxygens	46.5	46.5	46.5
Li	0.05	0.05	
Si	7.95	7.83	7.95
Al	17.57	17.61	17.58
Cr		0.01	
Ti	0.13	0.13	0.07
Fe^{2+}	3.12	3.25	2.26
Mn	0.01	0.01	0.01
Ni		0.00	
Zn	0.07	0.07	0.99
Mg	0.78	0.78	0.76
Ca			
Na		0.01	
K			
ΣCations	29.69	29.76	29.62

Values of oxides as wt%

Li only included in cation proportions

Cation normalization based on 46.5 oxygens

Campolungo metapelites of the Simano nappe, Lepontine Alps

The Simano nappe, outcropping in the Lepontine (central) Alps, represents part of the former European margin. It is comprised of a basement of predominantly Paleozoic orthogneisses, overlain by a metasedimentary sequence ranging in age from the Permian to the Jurassic (Gieré et al., 2011). Here, staurolite is found in the lower sections of this metasedimentary cover, notably outcropping at Campolungo (Figure 2). It occurs in metapelites also containing muscovite, biotite, garnet, quartz, and kyanite, along with minor amounts of chlorite, plagioclase, tourmaline, rutile, and ilmenite. According to models by Gieré et al. (2011), upon entering the amphibolite facies at 450 °C and 4.7 kbar, these rocks are predicted to have approximately ~7.5 vol. % staurolite (Figure 7a). Its abundance decreases progressively until it is completely consumed at around 660 °C and 8.5 kbar, as other phases, including minor amounts of melt, are formed—particularly kyanite. The model further indicates that staurolite begins to regrow early along the retrograde metamorphic path. A second model of modal abundances by the same authors, which accounts for an evolving bulk-rock composition as components are sequestered, indicates that staurolite begins to form at approximately 510 °C and 7.0 kbar during prograde metamorphism. Its abundance peaks at around 590 °C and 8.0 kbar, before being consumed at the expense of kyanite and melt formation between 660–630 °C and 8.5–6.5 kbar. Staurolite subsequently regrows under retrograde conditions (Figure 7b).

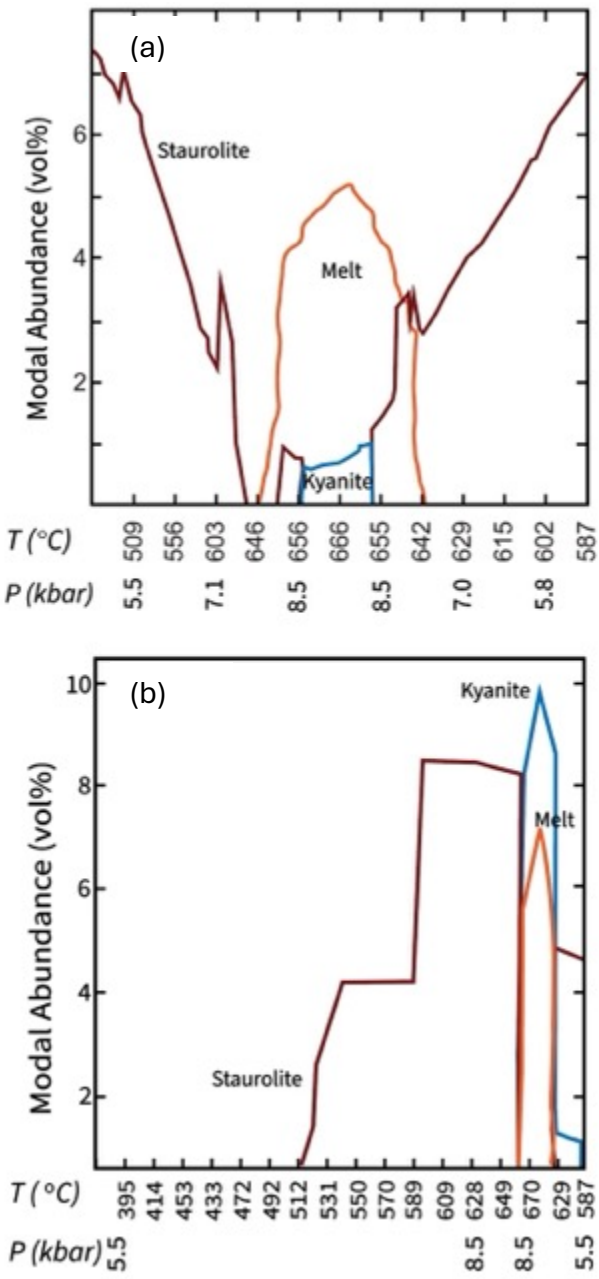

Figure 7. (a) Diagram showing the modal abundances of staurolite, kyanite, and melt (in vol.%) in fixed-bulk-rock composition metapelites (sample Leit 8) from Campolungo; curves for other phases are omitted for simplicity. (b) Diagram illustrating a model that accounts for an evolving bulk-rock composition during metamorphism, as components are sequestered by stable phases (specifically by garnet in this model; see Gieré et al., 2011). Both diagrams are modified from Gieré et al. (2011); diagram (a) is based on the P-T metamorphic path modeled by the same authors.

Monte Rosa Nappe, central Alps

The Monte Rosa nappe, outcropping in the central Alps, consists of polymetamorphic pre-Variscan basement and Permian-age granitic intrusions (Vaughan-Hammon et al., 2021) (Figure 2). This unit represents a fragment that rifted from the European margin during the Cretaceous (Stampfli et al., 2002) and was subsequently accreted into the Penninic pile during the Alpine orogeny. Within the Monte Rosa metapelites, staurolite appears as small blasts within distinct domains containing chloritoid, paragonite and phengite, whereas assemblages outside these domains consist of garnet, chlorite, white mica, and fine-grained quartz. These domains are interpreted as former contact metamorphic andalusite porphyroblasts that formed near Permian granitic intrusions (Figure 8a). The porphyroblasts were subsequently pseudomorphed by staurolite-bearing assemblages at peak metamorphic conditions during the Eocene (~42.6 Ma) high-pressure Alpine orogenesis (Vaughan-

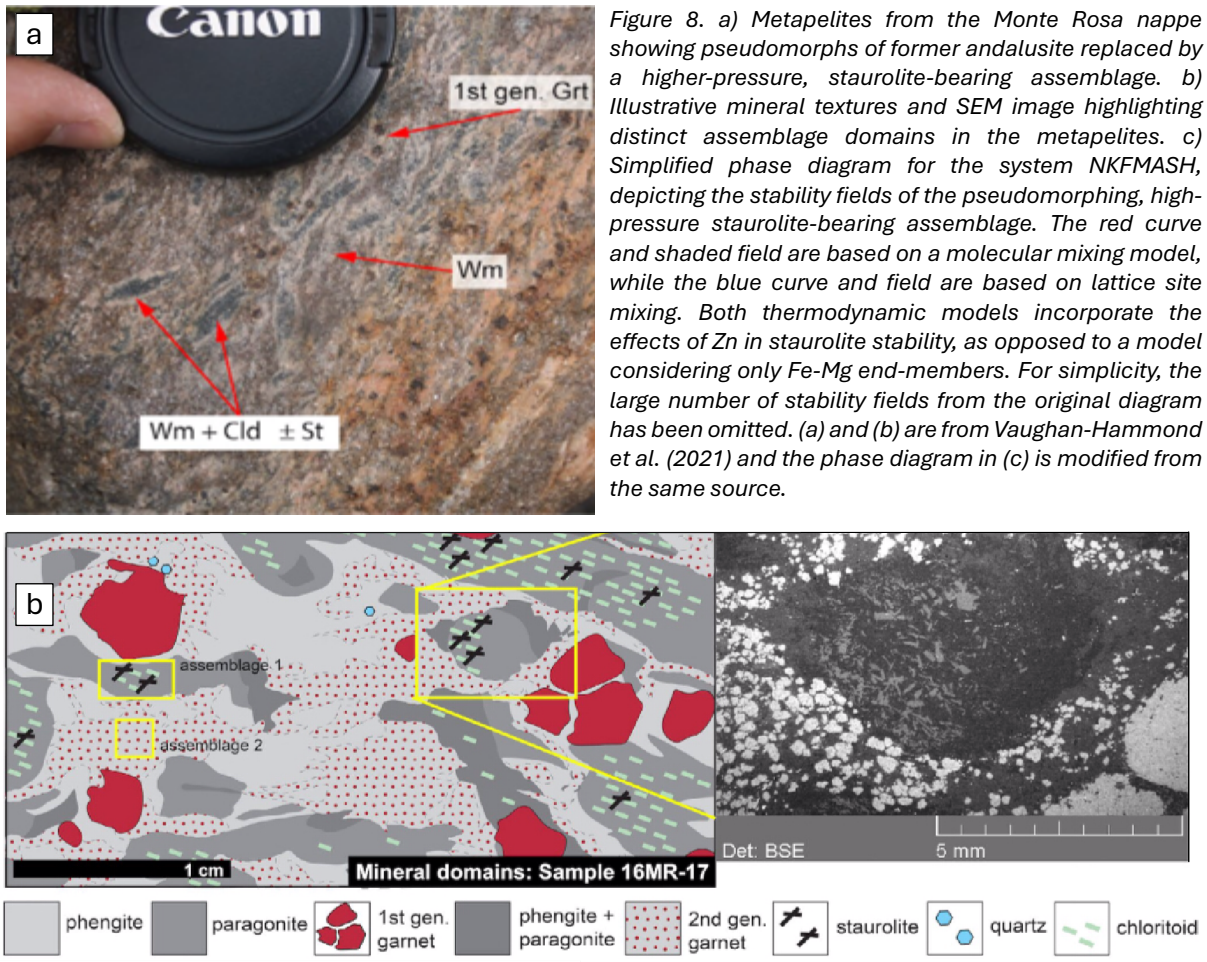

Figure 8. a) Metapelites from the Monte Rosa nappe showing pseudomorphs of former andalusite replaced by a higher-pressure, staurolite-bearing assemblage. b) Illustrative mineral textures and SEM image highlighting distinct assemblage domains in the metapelites. c) Simplified phase diagram for the system NKFMASH, depicting the stability fields of the pseudomorphing, high-pressure staurolite-bearing assemblage. The red curve and shaded field are based on a molecular mixing model, while the blue curve and field are based on lattice site mixing. Both thermodynamic models incorporate the effects of Zn in staurolite stability, as opposed to a model considering only Fe-Mg end-members. For simplicity, the large number of stability fields from the original diagram has been omitted. (a) and (b) are from Vaughan-Hammond et al. (2021) and the phase diagram in (c) is modified from the same source.

Hammon et al., 2021). Thermodynamic modelling by Vaughan-Hammon et al. (2021) based on two different mixing modes places the stability field of the studied staurolite-bearing assemblages (pseudomorphs afters andalusite) at 16 ± 1 kbar, 600 ± 5°C and 16 ± 2 kbar, 585 ± 15°C (Figure 8c).

Contact aureole of the Vedrette di Ries pluton

Staurolite is found within the contact metamorphic aureole of the Vedrette di Ries pluton (Figure 2), an Oligocene-aged intrusion located in the eastern Italian Alps. This pluton has intruded a polymetamorphic basement belonging to the Austroalpine nappes, which experienced both pre-Alpine and Alpine metamorphic events (Cesare, 1994). In these metapelites, sillimanite pseudomorphs have replaced andalusite during prograde contact metamorphism. Broken down to form the Fe-rich spinel hercynite within the sillimanite crystals, staurolite here it occurs as small, sparse, and resorbed inclusions. In contrast, abundant euhedral staurolite inclusions are preserved within relict andalusite (Figure 9a) (Cesare, 1994). The calculated sequence of reactions, supported by field observations by the same author, indicates an upper *T* stability limit for staurolite between 585°C to 655°C, and a maximum *P* of ~3.75 (Figure 9b).

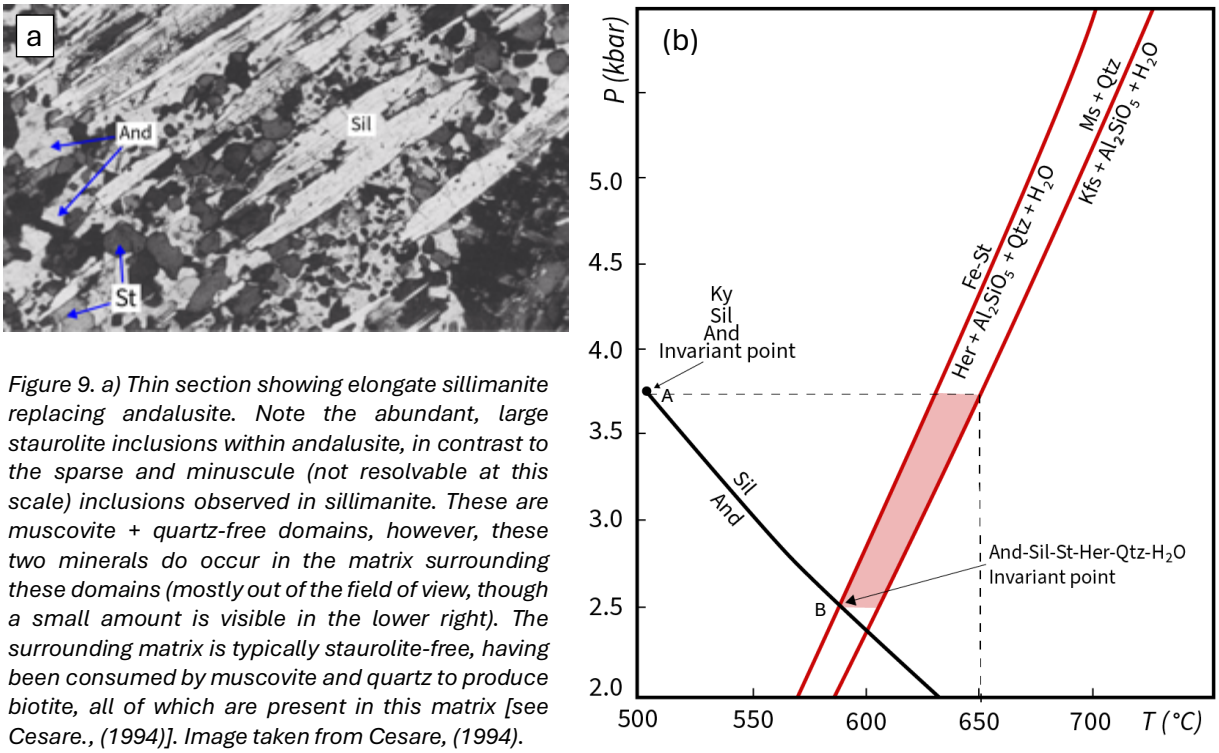

Figure 9. a) Thin section showing elongate sillimanite replacing andalusite. Note the abundant, large staurolite inclusions within andalusite, in contrast to the sparse and minuscule (not resolvable at this scale) inclusions observed in sillimanite. These are muscovite + quartz-free domains, however, these two minerals do occur in the matrix surrounding these domains (mostly out of the field of view, though a small amount is visible in the lower right). The surrounding matrix is typically staurolite-free, having been consumed by muscovite and quartz to produce biotite, all of which are present in this matrix [see Cesare., (1994)]. Image taken from Cesare, (1994).

b) Equilibrium curves for the simplified FASH and KFASH systems. The shaded field represents staurolite-hercynite (Her)-bearing metapelites. Given that andalusite is preserved metastably in the assemblage, and that the staurolite breakdown reaction took place within the sillimanite stability field (assuming no large overstepping of the reaction), the upper pressure stability range of this assemblage has been constrained by the andalusite maximum pressure limit, at point A. Similarly, the equilibrium assemblage St-Her-And-Sil-Qtz-H_2O (point B) constrains the lower pressure stability limit. Additionally, because muscovite + quartz are present in these metapelites, but not K-feldspar, the higher temperature equilibrium curve constrains the upper temperature limit (Cesare., 1994). Supported by field observation, this model provides compelling P-T estimates of staurolite breakdown at low pressures. Diagram modified from Cesare., (1994).

Discussion

The studies presented so far have shown that staurolite occurs along the entire length of the Alps, in a variety of metapelitic compositions, at times associated with multiple metamorphic events—both pre-Alpine and Alpine—, forming in regional but also associated with contact metamorphic regimes, and across most paleotectonic domains—from the European margin, internal massifs and Penninic Oceans, to the Austroalpine basement. These studies have also provided a number of bulk rock compositions for staurolite bearing metapelites and *P-T* stability ranges of 2.5 to 16 ± 1 kbar and 460 to 666 °C for staurolite in these rocks. The following discussion examines and compares the influence of the major components Al and Fe on the stability of staurolite across some of the metapelitic compositions presented earlier, as a function of their relative ratios. This is followed by a brief assessment on the utility of staurolite-

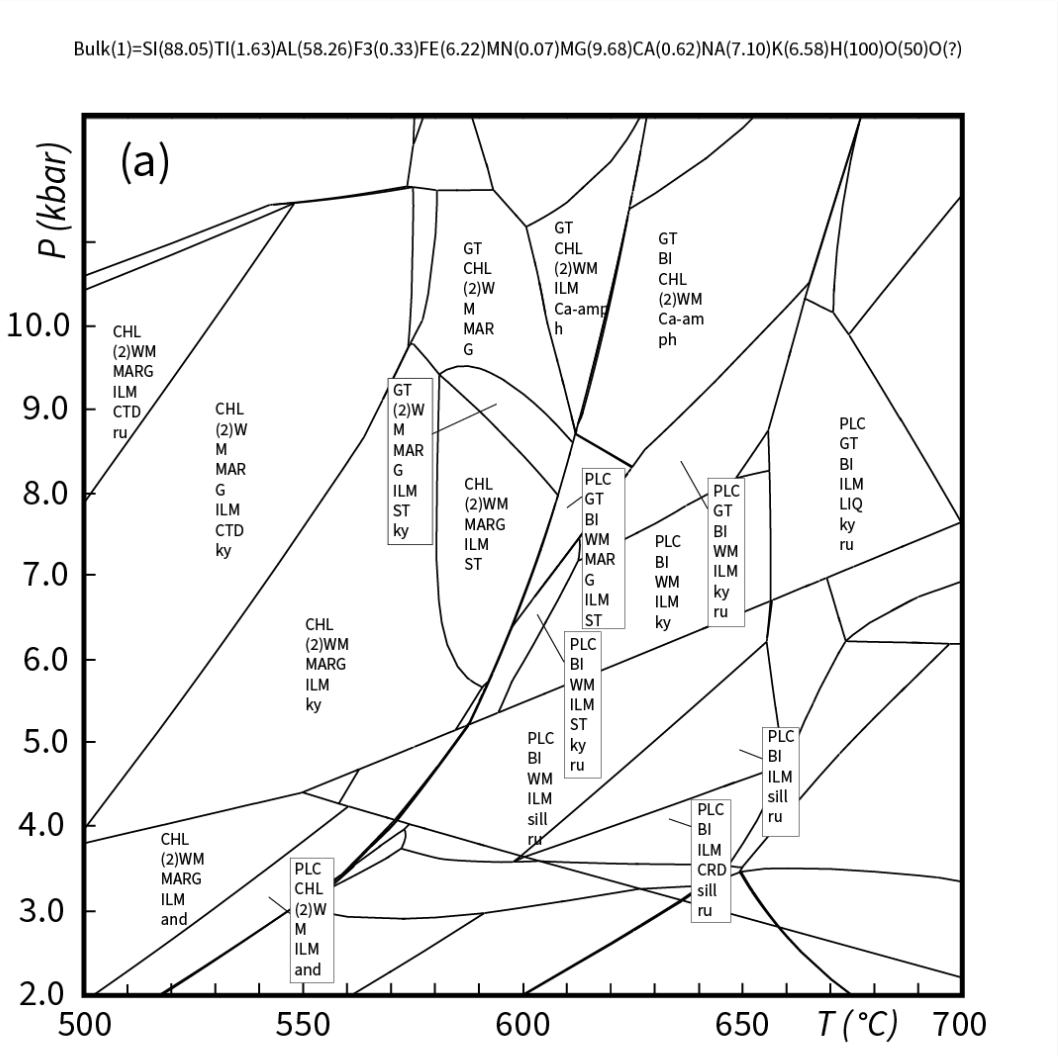

Figure 10. Pseudosection calculated for sample MF161 from Janots et al. (2008) in the system MnNCKFMASHTO. The bulk composition on a wt% basis used for this provided in Table 1. Complete recalculated data is presented in Table S1 in the supplementary material.

Al_2SiO_3 assemblages, as previously described, in interpreting the sequence and conditions of metamorphism in Alpine metapelites.

Relative influence of Al, Fe, and Mg on staurolite stability

Although the stability ranges are naturally expected to vary as a result of the specifics of the thermodynamic modeling approach, the bulk rock composition of the metapelite

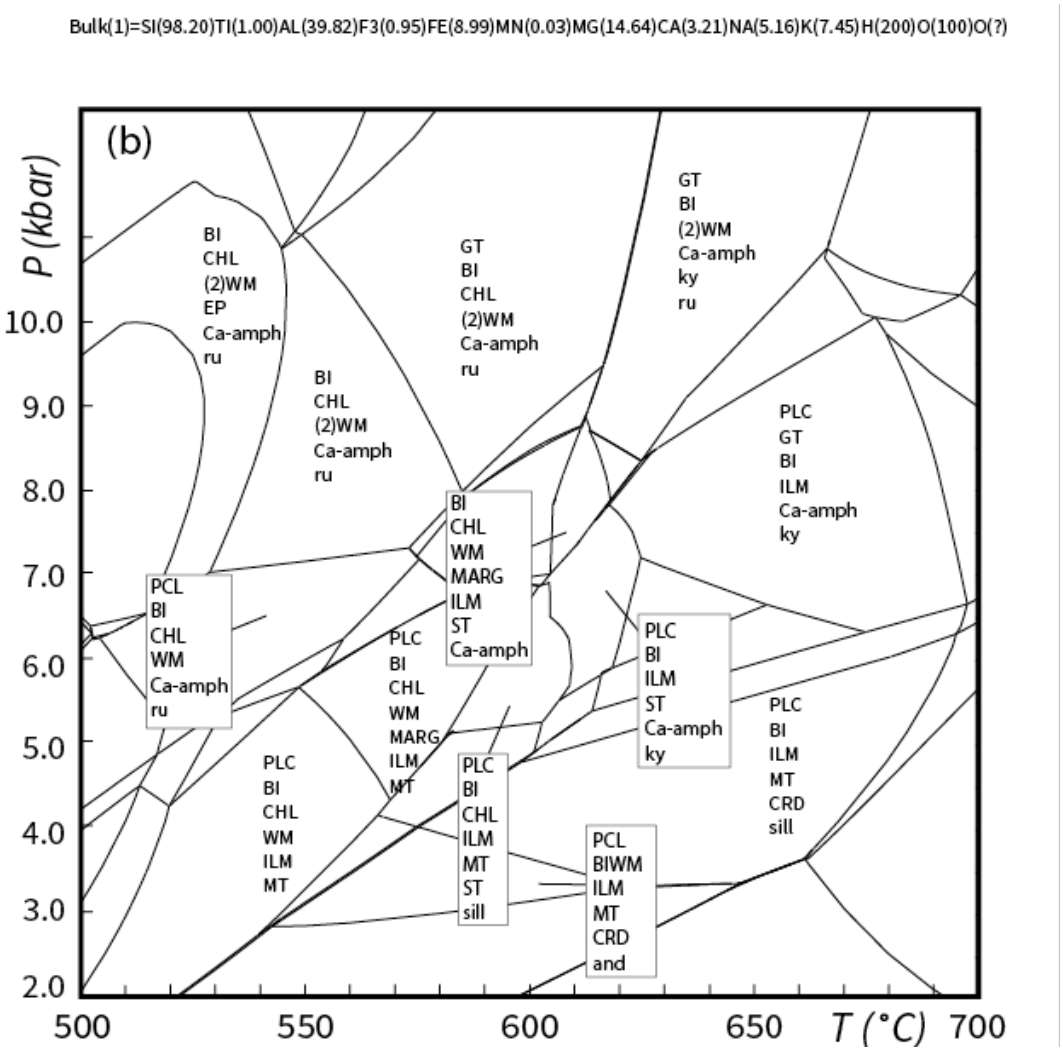

Figure 11. Pseudosection for sample MF307 in the system MnNCKFMASHTO from Janots et al. (2008). Complete recalculated data is presented in table S2 in the supplementary material.

should, *all things being equal*, primarily accounts for this variation. Figure 10, Figure 11 and Figure 12 show pseudosections calculated for this thesis on three metapelites based on the bulk rock compositions from Janots et al. (2008). Together with that calculated by Gaidies et al. (2008), a phase diagram has been constructed showing superimposed staurolite stability fields in *P-T* space, Figure 13. When considering these compositions plotted in AFM space (Figure 14), indeed, the effects of the proportions of these components on the stability of staurolite is noticeable. Composition MF307 has the highest MgO/(FeO* + MgO) ratio (0.61, Table 3) and lowest Al_2O_3/(FeO* + MgO) ratio (0.36), resulting in the most reduced staurolite stability. As both Fe and Al proportions

increase toward the composition MF315, the stability range expands. However, Figure 13, along with the ternary plot in Figure 14, further illustrates the relative contributions of Fe and Al to this expansion, suggesting that Fe has a greater influence than Al in stabilizing staurolite. Notably, while MF161 and MF307 exhibit a substantial difference in Al proportions, the variation in P-T range is relatively minor. Conversely, samples 29F03B and MF307 show a *small difference* in Al_2O_3/(FeO* + MgO) (0.45 vs. 0.36, respectively), yet a larger difference in MgO/(FeO* + MgO) (0.35 vs. 0.61), which translates to a significant change in stability range. The same is true when comparing the *P-T* range of MF161 and MF315 in which Fe proportions increase while Al remains relatively constant. In other words, in these Alpine metapelites, a relative increase in Fe results in greater staurolite stability in *P-T* space than a similar relative increase in Al.

The significance of Fe in controlling staurolite stability is also illustrated in the

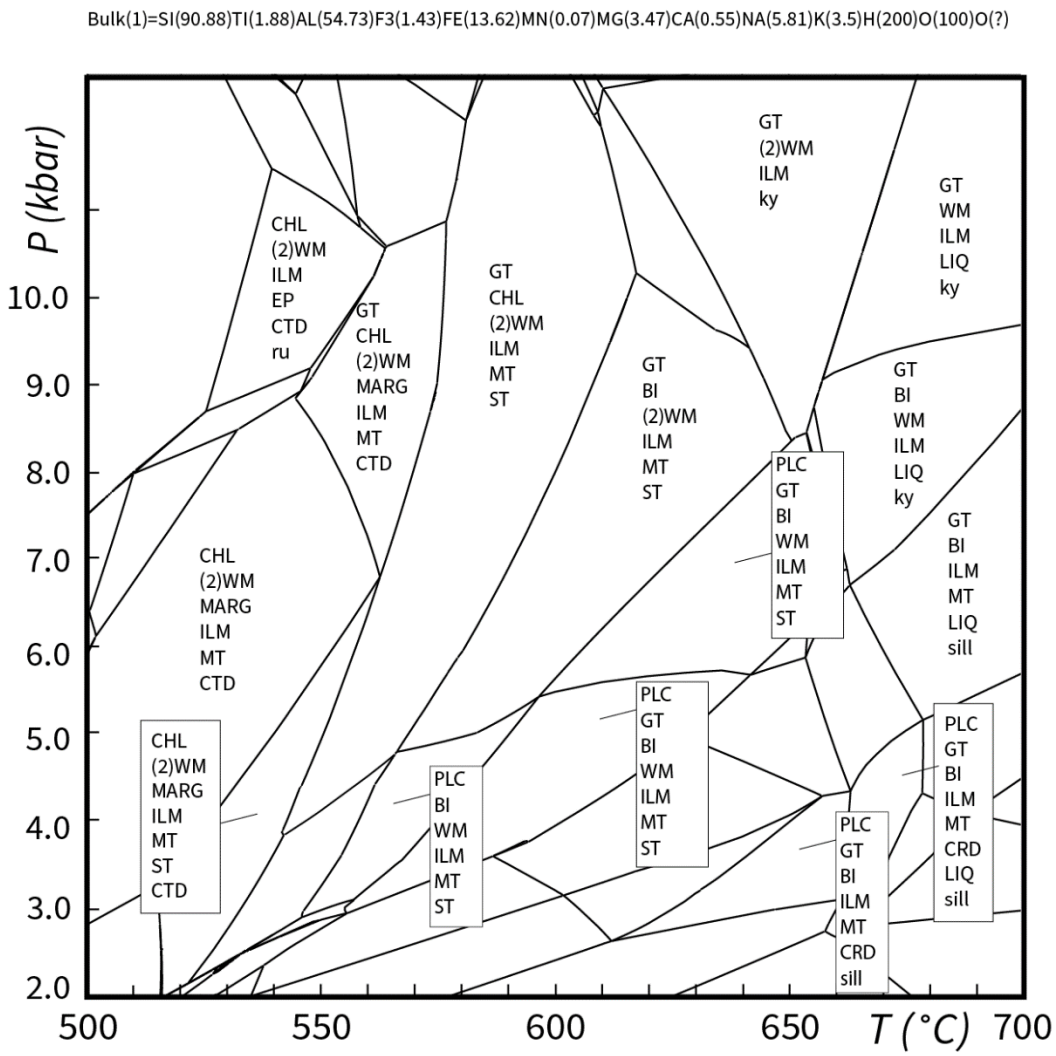

Figure 12. Pseudosection for sample MF315 in the system MnNCKFMASHTO from Janots et al. (2008). Complete recalculated data is presented in table S3 in the supplementary material.

petrogenetic grid in Figure 5 (where Fe-chloritoid gives way to Fe-staurolite at the lowest *T)*. The ternary chemographics of Figure 6 should corroborate this for the common metapelites. These ternary diagrams also show the limitations of Mg enrichment in staurolite Fe-Mg solid solution, and thus a corresponding reduction of *P-T* range in high MgO/(FeO* + MgO*)* metapelites.

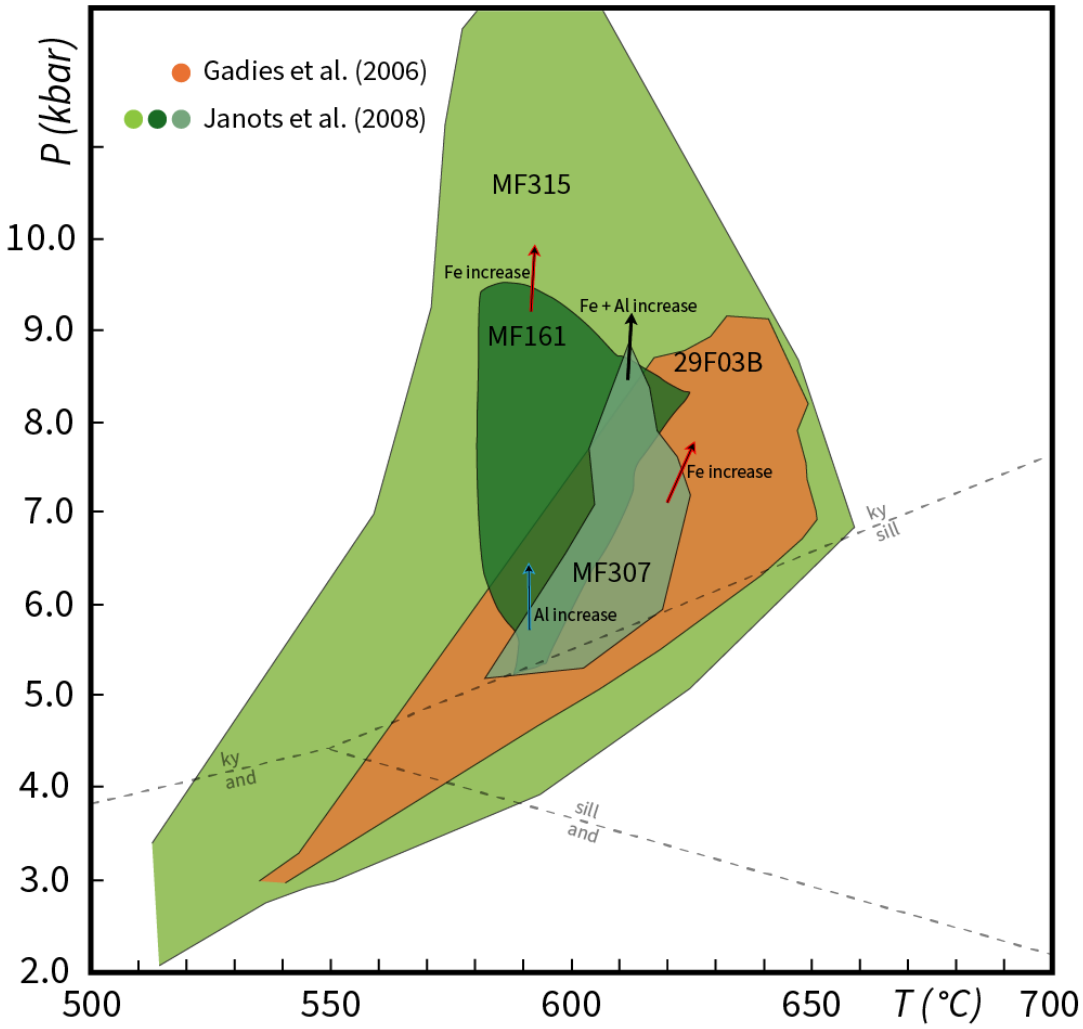

Figure 13. Staurolite stability fields superimposed in P-T space. Arrows indicate the P-T range expansion as a function of relative increases in only Fe and only Al between metapelitic compositions. Red arrows indicate the difference in range expansion from one field to the next when Fe proportion increases and Al remains approximately constant; blue arrows indicate the opposite (see AFM plot in Fig. 14 below). The stability field for sample 29F03B was calculated by Gadies et al. (2006) using PERPLEX. However, when the same composition is input into Theriak/Domino and using same a-X data as with the rest of the samples in this phase diagram, the trend discussed above becomes even more consistent. The slope of the arrows is arbitrary and thus unrelated to P-T; they are only intended for ease of visualization. Full pseudosection for sample 29F03B can be found in Fig. 16 in Gaidies et al. (2006). Aluminosilicate metastable curves are from the pseudosection in Figure 10.

Petrographical evidence in staurolite-Al_2SiO_5 relations for polymetamorphism and tectonic evolution

The Monte Rosa metapelites studied by Vaughan-Hammond et al. (2021) (see Figure 2) contain staurolite-bearing assemblages that have pseudomorphed andalusite porphyroblasts (Figure 8a, b). The authors reported that these metapelites were intruded by granitic magmas during the Permian, leading to the formation of the original andalusite, which occurs adjacent to the granitic bodies in these rocks. Andalusite was pseudomorphed by staurolite-bearing assemblages during Alpine orogenesis in the Eocene, subjecting these rocks to a new, higher-P metamorphic regime. Similarly, the metapelites studied by Cesare (1994) surrounding the Vedrette di Ries pluton also experienced polymetamorphism. However, here staurolite seems to predate the formation of the Al_2SiO_5 polymorphs andalusite and sillimanite, that resulted from the

Oligocene-age Vedrette di Ries tonalitic intrusion, with sillimanite clearly consuming both staurolite and andalusite (Figure 9a; see the sketch of this photomicrograph in Fig. 2b of Cesare, 1994), as temperatures continued to increase.

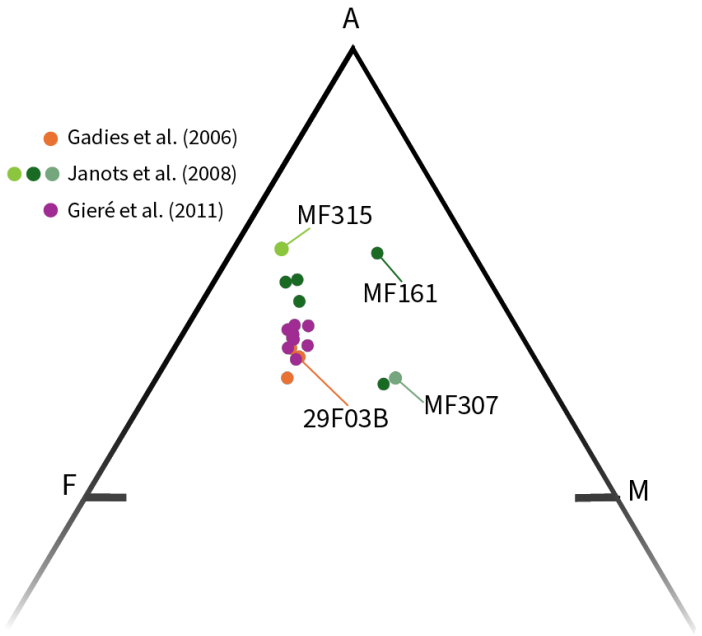

Figure 14. A(K)FM ternary projection showing the variability in metapelite compositions. See Table S4 and S5 (and Fig. S1) in supplementary material for recalculated compositions and plotting method.

These observations illustrate the utility of staurolite–Al_2SiO_5 relationships as indicators of both metamorphic regime and the chronological evolution of Alpine rocks. In the Monte Rosa metapelites, they record an initial low-pressure contact metamorphism during the Permian, a period of pronounced extensional tectonics in the region (Froitzheim and Klug, 2021; Zanchetta et al., 2024), likely linked to the incipient rifting of the Briançonnais microcontinent from the European margin. This was followed by the accretion of the Briançonnais block to the Alpine wedge, later subjected to higher-pressure metamorphism during the Eocene. In the basement metapelites of the Austroalpine domain (intruded by the Vedrette di Ries tonalite), in contrast, staurolite-Al_2SiO_5 relationships first record pre-Alpine (Variscan?) and Alpine metamorphism, overprinted by a younger contact metamorphism during emplacement of the Vedrette di Ries tonalitic intrusion. This intrusion is associated with a brief phase of extensional, post-collisional tectonics (Cesare, Fioretti, & Rosenberg, 2004).

	Sample			
	29F03B	MF161	MF307	MF315
Al_2O_3/(FeO* + MgO)	0.45	1.19	0.36	1.24
FeO*/MgO	1.85	0.68	0.65	4.13
MgO/(FeO* + MgO)	0.35	0.60	0.61	0.20
FeO*/(Al_2O_3 + MgO)	0.81	0.23	0.40	0.56

Table 3. Ratios of the AFM components. Calculated from values in Table S4 in supplementary material.

Lithium

As mentioned in the introduction, staurolite in metapelites can accommodate significant amounts of Li. However, in the absence of staurolite in the assemblage, Li is redistributed into other phases, typically following the order: staurolite > cordierite > biotite > muscovite > garnet > chloritoid (Dutrow et al., 1986). By determining the P-T stability range of staurolite as a function of bulk rock composition, we can also better infer Li mobility during metamorphism, as its release into fluids or melts is largely controlled by the stability of the host phase. Studying the behaviour of staurolite in metapelites can provide a better understanding of the portion of the Li cycle that traverses the metamorphic domain.

Conclusions

Staurolite is a medium-grade, hard, prismatic and largely porphyroblastic mineral that occurs in metapelites worldwide, both in regional and contact metamorphic rocks. Although it has a complex chemistry, it is highly favoured in aluminous and Fe-rich rocks and it is typically associated with other medium- to high-grade metamorphic minerals, including biotite, garnet, and the aluminosilicates.

Staurolite in metapelites is widespread across the Alps, of different ages, orogenic events, and geological settings, not only illustrating the complexity of Alpine formation, but also the diverse nature of this mineral; with the data from the literature and thermodynamic modelling indicating a range of staurolite stability of 2.5 to 16 ± 1 kbar and 460 to 666 °C. Additionally, thermodynamic modelling of staurolite-bearing bulk-rock compositions reveals the importance of major element proportions in defining the stability range of staurolite in *P-T* space. The results indicate that Fe has a greater effect relative to Al in expanding the *P-T* stability range of staurolite. This emphasizes the significance of bulk-rock composition, and, importantly, of FeO* / MgO proportions in the interpretation of metamorphic grade in staurolite-bearing metapelites. Although a much larger sample size and with greater variability is needed for more conclusive results.

Staurolite-Al_2SiO_5 polymorph relations record the various metamorphic regimes experienced by various Alpine domains. These range from pre-Alpine, low-pressure contact metamorphism to regional, high-pressure Alpine metamorphism and, elsewhere, the reverse sequence—progressing from regional pre-Alpine through Alpine to post-collisional contact metamorphism during exhumation. This reflects the varied metamorphic history of the Alps.

In addition to its significance in the reconstruction of Alpine geology, given the role that staurolite plays as a Li host, a metal of growing significance, understanding its occurrence and behaviour can provide clues into the broader Li cycle.

Acknowledgements

I would like to thank my supervisor Paola Manzotti for her patience, time and expertise. The quality of her attention and advice is truly exceptional. I would also like to thank all of my family for their constant support and encouragement.

Bibliography

Albee, A.L., 1972. Metamorphism of Pelitic Schists: Reaction Relations of Chloritoid and Staurolite. GSA Bulletin 83, 3249–3268. https://doi.org/10.1130/0016-7606(1972)83[3249:MOPSRR]2.0.CO;2

Blatt, H., Tracy, R.J., Owens, B.E., 2006. Petrology: igneous, sedimentary and metamorphic, 3. ed., [Nachdr.]. ed. Freeman, New York.

Borisova, E.B., Baltybaev, Sh.K., Connolly, J.A.D., 2022. Staurolite in Metabasites: P–T–X Parameters and the Ratios of Major Components as Criteria of Staurolite Stability. Petrology 30, S53–S71. https://doi.org/10.1134/S0869591123010034

Bringhurst, K.N., Griffen, D.T., 1986. Staurolite-lusakite series. II. Crystal structure and optical properties of a cobaltoan staurolite. American Mineralogist 71, 1466–1472.

Cesare, B., 1994. Hercynite as the product of staurolite decomposition in the contact aureole of Vedrette di Ries, eastern Alps, Italy. Contr. Mineral. and Petrol. 116, 239–246. https://doi.org/10.1007/BF00306495

Cesare B., Fioretti A. & Rosenberg C. (2004) - The periadriatic intrusion of Vedrette di Ries - Rieserferner (eastern Alps): petrology, emplacement mechanisms and contact aureole. 32nd IGC, B17 Field Trip Guide Book. Published by APAT – Italian Agency for the Environmental Protection and Technical Services - Rome, 36pp.

Condie, K.C., 1993. Chemical composition and evolution of the upper continental crust: Contrasting results from surface samples and shales. Chemical Geology 104, 1–37. https://doi.org/10.1016/0009-2541(93)90140-E

De Capitani, C., Petrakakis, K., 2010. The computation of equilibrium assemblage diagrams with Theriak/Domino software. American Mineralogist 95, 1006–1016. https://doi.org/10.2138/am.2010.3354

Dutrow, B.L., Holdaway, M.J., Hinton, R.W., 1986. Lithium in staurolite and its petrologic significance. Contr. Mineral. and Petrol. 94, 496–506. https://doi.org/10.1007/BF00376341

Froitzheim, N., Klug, L., 2021. Permian rifting and detachment faults and their role in Alpine collisional tectonics. EGU General Assembly Conference Abstracts EGU21-16307. https://doi.org/10.5194/egusphere-egu21-16307

Gaidies, F., Abart, R., De Capitani, C., Schuster, R., Connolly, J.A.D., Reusser, E., 2006. Characterization of polymetamorphism in the Austroalpine basement east of the Tauern Window using garnet isopleth thermobarometry. Journal Metamorphic Geology 24, 451–475. https://doi.org/10.1111/j.1525-1314.2006.00648.x

Gieré, R., Rumble, D., Günther, D., Connolly, J., Caddick, M.J., 2011a. Correlation of Growth and Breakdown of Major and Accessory Minerals in Metapelites from Campolungo, Central Alps. Journal of Petrology 52, 2293–2334. https://doi.org/10.1093/petrology/egr043

Gieré, R., Rumble, D., Günther, D., Connolly, J., Caddick, M.J., 2011b. Correlation of Growth and Breakdown of Major and Accessory Minerals in Metapelites from Campolungo, Central Alps. Journal of Petrology 52, 2293–2334. https://doi.org/10.1093/petrology/egr043

Gromet, L.P., Haskin, L.A., Korotev, R.L., Dymek, R.F., 1984. The “North American shale composite”: Its compilation, major and trace element characteristics. Geochimica et Cosmochimica Acta 48, 2469–2482. https://doi.org/10.1016/0016-7037(84)90298-9

Hawthorne, F.C., Ungaretti, L., Oberti, R., Caucia, F., Callegari, A., 1993. The crystal chemistry of staurolite; I, Crystal structure and site populations. The Canadian Mineralogist 31, 551–532.

Ibarguchi, J., Mendia, M., Girardeau, J., 1991. Mg- and Cr-rich staurolite and Cr-rich kyanite in high-pressure ultrabasic rocks (Cabo Ortegal, northwestern Spain). American Mineralogist 76, 501–511.

Janák, M., Uher, P., Ravna, E.K., Kullerud, K., Vrabec, M., 2015. Chromium-rich kyanite, magnesiostaurolite and corundum in ultrahigh-pressure eclogites (examples from Pohorje Mountains, Slovenia and Tromsø Nappe, Norway). ejm 27, 377–392. https://doi.org/10.1127/ejm/2015/0027-2436

Janots, E., Engi, M., Berger, A., Allaz, J., Schwarz, J. -O., Spandler, C., 2008. Prograde metamorphic sequence of REE minerals in pelitic rocks of the Central Alps: implications for allanite–monazite–xenotime phase relations from 250 to 610 °C. Journal Metamorphic Geology 26, 509–526. https://doi.org/10.1111/j.1525-1314.2008.00774.x

Miyake, A., 1985. Zn-rich staurolite from the Uvete area, central Kenya. Mineral. mag. 49, 573–578. https://doi.org/10.1180/minmag.1985.049.353.11

Pattison, D.R.M., Spear, F.S., 2018. Kinetic control of staurolite–Al_2SiO_5 mineral assemblages: Implications for Barrovian and Buchan metamorphism. Journal Metamorphic Geology 36, 667–690. https://doi.org/10.1111/jmg.12302

Prenzel, J.D., Abart, R., 2009. Garnet reaction rims from the breakdown of Staurolite in polymetamorphic micashists from the Rappold complex, Austroalpine basement, Eastern Alps. Miner Petrol 97, 189–201. https://doi.org/10.1007/s00710-009-0083-0

Spear, F.S., Cheney, J.T., 1989. A petrogenetic grid for pelitic schists in the system SiO2-Al2O3-FeO-MgO-K2O-H2O. Contributions to Mineralogy and Petrology 101, 149–164. https://doi.org/10.1007/BF00375302

Stampfli, G.M., Borel, G.D., Marchant, R., Mosar, J., 2002. Western Alps geological constraints on western Tethyan reconstructions. J.Virt.Ex 08. https://doi.org/10.3809/jvirtex.2002.00057

Symmes, G.H., Ferry, J.M., 1991. Evidence from mineral assemblages for infiltration of pelitic schists by aqueous fluids during metamorphism. Contr. Mineral. and Petrol. 108, 419–438. https://doi.org/10.1007/BF00303447

Vaughan-Hammon, J.D., Luisier, C., Baumgartner, L.P., Schmalholz, S.M., 2021. Peak Alpine metamorphic conditions from staurolite-bearing metapelites in the Monte Rosa nappe (Central European Alps) and geodynamic implications. Journal Metamorphic Geology 39, 897–917. https://doi.org/10.1111/jmg.12595

Winter, J.D., 2014a. Principles of igneous and metamorphic petrology, 2. ed., Pearson new internat. ed. ed. Pearson Education, Harlow.

Yardley, B.W.D., MacKenzie, W.S., Guilford, C., 1990. Atlas of metamorphic rocks and their textures. Longman scientific and technical, Harlow (GB).

Zanchetta, S., Crippa, C., Zanchi, A., Montemagni, C., 2024. The Val Biandino Intrusive Suite (central Southern Alps, N Italy): new geochronological and geochemical data on the Early Permian magmatic activity in the Southalpine Domain. Swiss Journal of Geosciences 117, 7. https://doi.org/10.1186/s00015-024-00457-4

Supplementary Material

Appendix S1. A-X models included and activated in the database used for Theriak/Domino thermodynamic modelling for pseudosections.

PLC1 - HP 2003 ternary, C1 field (read HP 1996 (Am.Min.) and 2003)
GT07W2- White et al. 2007; adjusted W's and a's as in tc331; tc331 'preferred' model.
BI07 - White et al. 2007 (use with GT07)
CHL - Mahar et al. 1997/HP 1998
WM02 - Coggon & Holland, 2002, with their prl and margarite members excluded
ILM05 - White et al., 2000,2005 (for Mn system)
MTSP02 - White et al., 2002
CAMP - Diener et al., 2007
OAMP - Diener et al., 2007
CPX07 - Green et al., 2007
OPX - White et al., 2002; on top of HP 1999
TA98 - HP98
EP98 - HP98
CRD - HP98
ST - HP98
CTD - HP98
LIQtc - White et al. 2007 melt model
OSM - Osumulite model as in TC file tc-NCKFMASHTO.txt

TABLE S1 Molar compositions for sample MF161 from Janots et al. (2008), recalculated from weight percent oxide values in Table 1.

	Sample MF161				
	Molecular weight (g/mol)	Cation count	Oxygen count	Moles of oxide	Moles of cations
SiO_2	60.08	1	2	88.05	88.05
TiO_2	79.87	1	2	1.63	1.63
Al_2O_3	101.96	2	3	29.13	58.26
FeO*	71.84	1	1	6.54	6.54
FeO	71.84	1	1	6.22	6.22
Fe2O3	159.7	2	3	0.33	0.65
MnO	70.94	1	1	0.07	0.07
MgO	40.3	1	1	9.68	9.68
CaO	56.08	1	1	0.62	0.62
Na_2O	61.98	2	1	3.55	7.10
K_2O	94.2	2	1	3.29	6.58

TABLE S2 Molar compositions for sample MF307 from Janots et al. (2008), recalculated from weight percent oxide values in Table 1.

	Sample MF307				
	Molecular weight (g/mol)	Cation count	Oxygen count	Moles of oxide	Moles of cations
SiO_2	60.08	1	2	98.20	98.20
TiO_2	79.87	1	2	1.00	1.00
Al_2O_3	101.96	2	3	19.91	39.82
FeO*	71.84	1	1	9.47	9.47
FeO	71.84	1	1	8.99	8.99
Fe_2O_3	159.7	2	3	0.47	0.95
MnO	70.94	1	1	0.03	0.03
MgO	40.3	1	1	14.64	14.64
CaO	56.08	1	1	3.21	3.21
Na_2O	61.98	2	1	2.58	5.16
K_2O	94.2	2	1	3.73	7.45

TABLE S3 Molar compositions for sample MF315 from Janots et al. (2008), recalculated from weight percent oxide values in Table 1.

	Sample MF315				
	Molecular weight (g/mol)	Cation count	Oxygen count	Moles of oxide	Moles of cations
SiO_2	60.08	1	2	90.88	90.88
TiO_2	79.87	1	2	1.88	1.88
Al_2O_3	101.96	2	3	27.36	54.73
FeO*	71.84	1	1	14.34	14.34
FeO	71.84	1	1	13.62	13.62
Fe2O3	159.7	2	3	0.72	1.43
MnO	70.94	1	1	0.07	0.07
MgO	40.3	1	1	3.47	3.47
CaO	56.08	1	1	0.55	0.55
Na_2O	61.98	2	1	2.90	5.81
K_2O	94.2	2	1	1.75	3.50

Table S4 Data based on molecular proportions calculated from Table 1 in the main text.

	Sample																		
	12F03	29F03B	35F03	MF161	MF307	MF315	APi0413	SPi0306	SMo0407	AMo0410	Leit 3	Leit 8	Leit 10	Leit 300	.eit 300a	Leit 400	Leit 400a	Leit 400b	Leit 900
A	0.09	0.07	0.08	0.20	0.09	0.22	0.10	0.14	0.20	0.12	0.09	0.09	0.08	0.09	0.09	0.07	0.11	0.12	0.07
F	0.12	0.10	0.14	0.07	0.09	0.14	0.12	0.12	0.15	0.10	0.11	0.13	0.10	0.11	0.11	0.09	0.12	0.12	0.10
M	0.06	0.05	0.07	0.10	0.15	0.03	0.17	0.04	0.06	0.05	0.05	0.06	0.05	0.05	0.05	0.05	0.06	0.07	0.05
Total	0.27	0.22	0.28	0.36	0.33	0.40	0.39	0.30	0.41	0.27	0.25	0.28	0.22	0.25	0.24	0.21	0.28	0.31	0.22
A%	33.17	31.25	26.57	54.29	26.60	55.39	25.19	47.87	48.41	43.57	36.22	33.25	35.51	37.30	35.18	33.73	38.25	38.13	30.68
F%	45.26	44.63	49.23	18.44	28.82	35.91	31.83	38.89	36.47	38.49	43.31	45.76	43.84	43.81	43.78	41.86	42.00	39.49	45.59
M%	21.57	24.11	24.20	27.27	44.58	8.70	42.98	13.25	15.12	17.94	20.47	20.99	20.65	18.89	21.04	24.41	19.75	22.38	23.73
A	0.33	0.31	0.27	0.54	0.27	0.55	0.25	0.48	0.48	0.44	0.36	0.33	0.36	0.37	0.35	0.34	0.38	0.38	0.31
M/FM	0.32	0.35	0.33	0.60	0.61	0.20	0.57	0.25	0.29	0.32	0.32	0.31	0.32	0.30	0.32	0.37	0.32	0.36	0.34

Cas1: A=Al2O3-3K20, FeO, MgO (projection from muscovite) on anhydrous basis

Table S5 Input data (extracted from table S4 above) for ternary plot in Figure 14 and plotting values for apices.

	(Fe)	(Mg)	(Al)	X	Y
	A	B	C		
	1	0	0	0	0
	0	1	0	1.15	0
	0	0	1	0.58	1
Sample					
12F03	0.45	0.22	0.33	0.44	0.33
29F03B	0.45	0.24	0.31	0.46	0.31
35F03	0.49	0.24	0.27	0.43	0.27
MF161a	0.18	0.27	0.54	0.63	0.54
MF307a	0.29	0.45	0.27	0.67	0.27
MF315a	0.36	0.09	0.55	0.42	0.55
APi0413	0.32	0.43	0.25	0.64	0.25
SPi0306	0.39	0.13	0.48	0.43	0.48
SMo0407	0.36	0.15	0.48	0.45	0.48
AMo0410	0.38	0.18	0.44	0.46	0.44
Leit 3	0.43	0.20	0.36	0.45	0.36
Leit 8	0.46	0.21	0.33	0.43	0.33
Leit 10	0.44	0.21	0.36	0.44	0.36
Leit 300	0.44	0.19	0.37	0.43	0.37
Leit 300a	0.44	0.21	0.35	0.45	0.35
Leit 400	0.42	0.24	0.34	0.48	0.34
Leit 400a	0.42	0.20	0.38	0.45	0.38
Leit 400b	0.39	0.22	0.38	0.48	0.38
Leit 900	0.43	0.24	0.31	0.45	0.31

Figure S1 Plotting parameters for ternary plot.